Nano Research

Open Access

Research Article

Architecting nanoconfined multiphase gels as a reprocessable and multistimuli-responsive 4D printing platform

Zewei Li[§], Yuzhu Cui[§], Shihao Zhou, Zongshu Li, Mingliang Zhao, Shuxue Wang, Yongxin Duan, Jianming Zhang, and Lu Zong ✉

Key Laboratory of Rubber-Plastics, Ministry of Education/Shandong Provincial Key Laboratory of Rubber-plastics, Qingdao University of Science & Technology, Qingdao 266042, China

§ Zewei Li and Yuzhu Cui contributed equally to this work.

Cite this article: *Nano Research*, **2026**, *19*, 94908644. https://doi.org/10.26599/NR.2026.94908644

ABSTRACT: Four-dimensional (4D)-printed shape memory gels (SMGs) have shown great potential for bionic scaffolds and soft robotics. However, their practical deployment is often limited by insufficient mechanical strength and reprocessability. Here, a nanoconfined multiphase gel strategy to develop reprocessable and multistimuli-responsive 4D-printed SMGs is proposed. The developed poly(vinyl alcohol) (PVA)/chitin nanocrystals (ChNC)/paraffin wax (PW) multiphase gel (PCPG) employs zwitterionic ChNC as interfacial stabilizers to construct a nanoconfined environment through abundant interfacial interactions, including hydrophobic interactions with the paraffin (PW) microphase and hydrogen bonding with the PVA gel matrix. These synergistic interactions lead to a remarkable enhancement in tensile strength (by ~ 50%, up to ~ 1 MPa). A high loading of phase-change PW (volume fraction > 70%) imparts outstanding shape memory properties and printability, with fixation and recovery ratios both exceeding 95%, along with high responsiveness to both thermal and acoustic stimuli. Importantly, the dynamically crosslinked network combined with efficient nanoconfinement enables excellent reprocessability, and the 4D-printed PCPG retains over 85% of its original mechanical and shape memory performance after ten reprocessing cycles. This strategy successfully merges nanoconfinement design with reprocessability, providing a sustainable platform for high-performance 4D-printed bionic scaffolds.

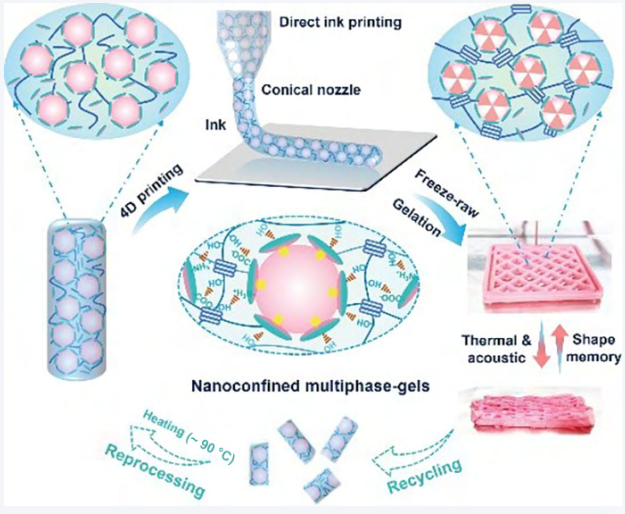

KEYWORDS: multiphase gel, shape memory, nanoconfined, reprocessability, four-dimensional (4D printing

1 Introduction

The burgeoning fields of implantable biomedical devices, tissue engineering, and regenerative medicine are increasingly reliant on advanced soft materials that offer dynamic functionality and structural adaptability, such as biomedical scaffolds and soft robots [1–3]. Shape memory gels (SMGs, including hydrogels [4], ionic gel [5], and multiphase organohydrogels gels [6]), a class of stimuli-responsive "soft-wet" materials capable of programmable shape morphing in response to external triggers (e.g., temperature, light, and pH), hold significant promise for applications such as dynamic tissue scaffolds and adaptive implants [7–9]. However, the practical deployment of existing SMGs is severely limited by their generally limited geometric complexity and lack of environmental sustainability [10].

Four-dimensional (4D) printing, which introduces a time dimension to three-dimensional (3D) printing, offers a transformative solution for constructing complex structures and enabling functional evolution in SMGs [11–13]. Among various printing techniques, extrusion-based direct ink writing is particularly attractive due to its simplicity and material adaptability, but its success heavily relies on the ink's high viscoelasticity and shear-thinning behavior [14, 15]. Recently, Pickering emulsion

Received: February 5, 2026; **Revised:** March 7, 2026
Accepted: March 16, 2026

✉Address correspondence to zonglu@qust.edu.cn

systems have emerged as ideal ink platforms by leveraging their high internal phase ratio and tunable interfaces [16]. These emulsions, stabilized by solid nanoparticles (e.g., nanosilica and nanocellulose) at the oil/water interface, form stable nanoconfined structures [17–20]. This not only enhances the interfacial adhesion between phases but also improves the overall mechanical performance through interfacial interactions (e.g., hydrogen bonding and hydrophobic effects) [21, 22]. Notably, when a crystallizable/meltable phase-change oil is used as the dispersed phase, the printed emulsion can exhibit thermally triggered shape memory functionality [23]. Nevertheless, current research on 4D-printed SMGs has predominantly prioritized printability, often at the expense of mechanical robustness and end-of-life recyclability.

The design of the gel matrix is paramount to achieving high-performance 4D-printed SMGs [24–26]. Multiphase SMGs, driven by a high-volume fraction (> 50%) of crystallizable/meltable microdomains, typically offer faster stimulus response and superior shape memory efficiency compared to systems relying solely on supramolecular interactions or dynamic covalent bonds, due to their distinct phase transition behavior [27–29]. Seminal work by Liu's group [18], for instance, demonstrated the power of architecting biomimetic multiphase structures. By constructing polymer networks within paraffin (PW) emulsions and incorporating nanofillers like nanoclays, they achieved impressive mechanical properties (fracture strength of 0.1–0.6 MPa) and exceptional shape memory performance (recovery ratio of ~ 98%). These milestones underscore that building stable and hierarchical crosslinked networks from the molecular to the micro-scale is an effective strategy for enhancing gel properties. However, these robust and multi-scale networks often rely on permanent or difficult-to-reverse crosslinks, which significantly sacrifice the gel's reprocessability. Therefore, integrating nanoconfinement effects to construct a 4D-printable gel that simultaneously possesses high mechanical strength, multistimuli-responsiveness, and excellent reprocessability remains a significant challenge.

Herein, we propose a nanoconfined multiphase gel strategy to develop a reprocessable and multistimuli-responsive 4D printing platform (Fig. 1(a)). A high internal phase Pickering emulsion gel (PCPG) composed of a poly(vinyl alcohol) (PVA) aqueous matrix, phase-change PW mirophase (volume fraction > 70%), and zwitterionic chitin nanocrystals (ChNC) as an interfacial stabilizer is systematically architected. Compared with other nanomaterials, amphoteric chitin nanocrystals achieve highly efficient emulsification across a wide pH range (Fig. 1(b)). Other nanomaterials, such as cellulose nanocrystals (CNCs) and cellulose nanofibers (CNFs), with an isoelectric point of ~ 4.2, gel in acidic media (pH = 4) [30], whereas aminated chitin nanofibers (ChNFs), with an isoelectric point of ~ 6.5, flocculate in alkaline media

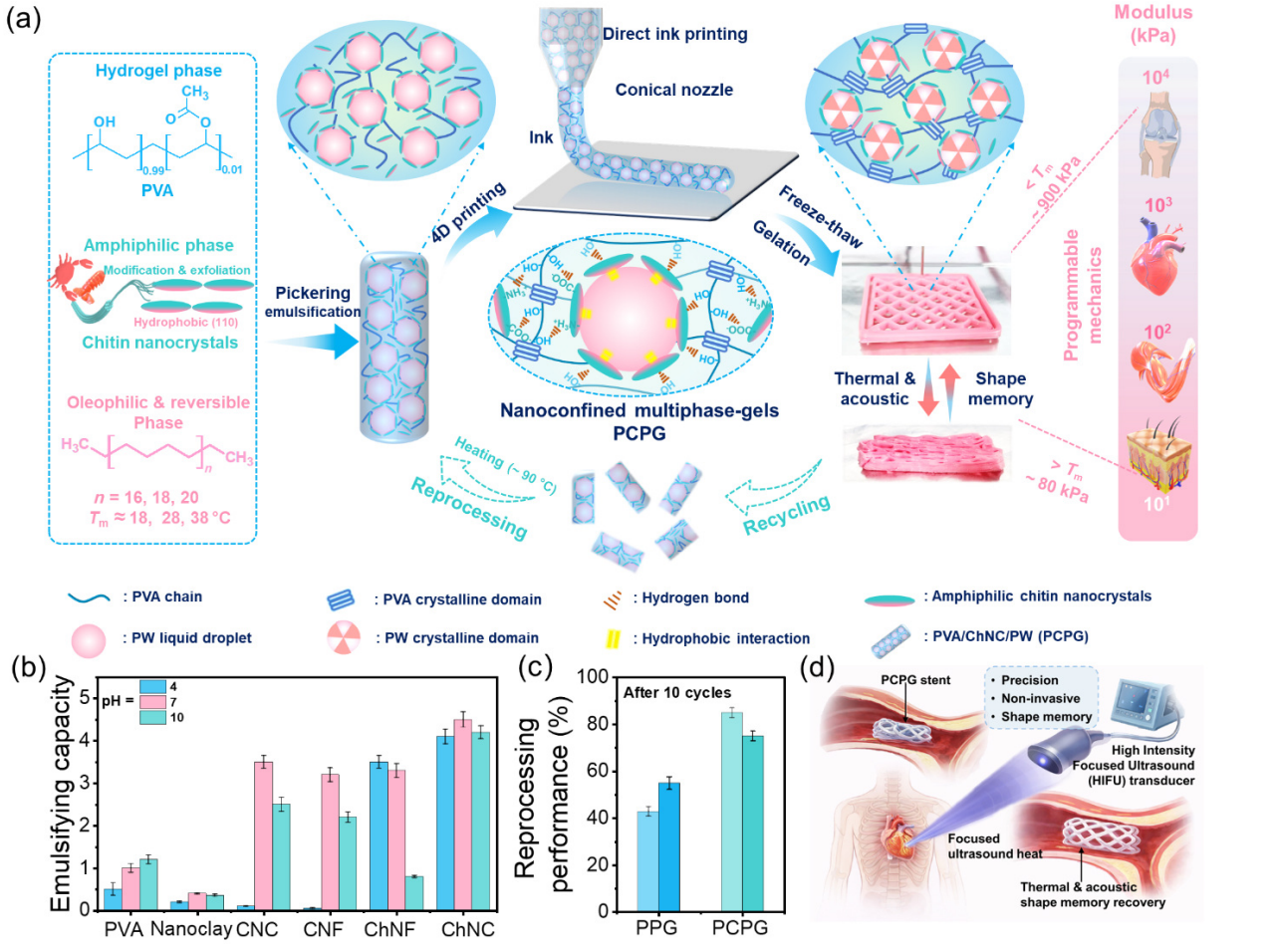

Figure 1 (a) Schematic diagram of the principle of architecting nanoconfined PCPG as a reprocessable and multistimuli-responsive 4D printing platform. (b) Emulsifying ability of different nanomaterial emulsifiers (PVA, PVA/nanoclay/PW, PVA/CNC/PW, PVA/CNF/PW, PVA/ChNF/PW, and PVA/ChNC/PW) at pH = 4, 7, and 10. (c) The reprocessability of PPG and PCPG is represented by the shape fixing rate (left column) and the mechanical property retention rate (right column), respectively. (d) High intensity focused ultrasound image of vascular stent *in vitro*.

(pH = 10) [31], thereby limiting their emulsification performance under these conditions. The zwitterionic ChNC forms a rigid network at the oil–water interface, creating a nanoconfined environment mediated by abundant interfacial interactions, hydrogen bonding with the PVA matrix and hydrophobic interactions with PW. The unique architecture synergistically enhances the tensile strength by approximately 50% (up to 1 MPa) compared to control gels. The high loading of PW not only imparts PCPG's outstanding thermal- and acoustic-responsive shape memory properties (fixation and recovery ratios both > 95%) but also provides the necessary viscoelasticity for high-fidelity 4D printing. Crucially, the physically crosslinked nature of the network, combined with the efficient nanoconfinement effect, enables exceptional reprocessability. The 4D-printed structures retain over 85% of their original mechanical and shape memory performance even after ten rigorous reprocessing cycles (Fig. 1(c)). It also shows suitability for *ex vivo* ultrasound application as a vascular stent (Fig. 1(d)). This work successfully merges the concepts of nanoconfinement engineering with circular material design, establishing a sustainable and high-performance platform for the next generation of 4D-printed bionic scaffolds and intelligent soft devices.

2 Results and discussion

2.1 Physical and chemical characterization of PCPG

Firstly, a high internal phase Pickering emulsion suitable for 4D printing was successfully prepared using a PVA aqueous solution as the continuous gel phase, phase change PW as the oil phase, and ChNC as the interfacial stabilizer. The 4D-printed gel was subsequently subjected to freeze–thaw cycles, ultimately yielding the PCPG with good mechanical strength. ChNC form a multi-cross-linked network at the oil–water interface and synergistically reinforces the gel matrix through hydrogen bonding with PVA and hydrophobic interactions with PW (the preparation and physicochemical characterization of ChNC are shown in Figs. S1 and S2 in the Electronic Supplementary Material (ESM)). The physicochemical properties of the PCPG were then systematically characterized and analyzed. The results indicated that the introduction of ChNC significantly increased the oil-to-water volume ratio (O/W) of the Pickering emulsion, reaching a maximum of 7.5/2.5, whereas the system without ChNC only achieved an O/W of 6.5/3.5 (Fig. S3 in the ESM). Concurrently, the presence of ChNC led to a noticeable reduction in the average droplet size (~ 4.8 μm) and a more uniform size distribution (Figs. 2(a) and 2(b))), primarily attributable to the significant steric hindrance that it imparts within the emulsion system. Furthermore, a series of Pickering emulsions were prepared by varying the ChNC content (0.5 wt.%, 1 wt.%, 2 wt.%, and 3 wt.%), and the oil droplet size was quantitatively analyzed using optical microscopy (Fig. 2(c), and Figs. S4 and S5 in the ESM). The results showed that the average droplet size reached a minimum at the ChNC concentration of 2 wt.%, indicating that the stable network formed by ChNC at the oil–water interface at this concentration is most conducive to the stable construction of the emulsified system. Based on this finding, the 2 wt.% ChNC were selected as the optimal emulsifier concentration to prepare Pickering emulsions with different O/W ratios (6/4, 7/3, and 7.5/2.5) for systematically investigating the effect of oil phase proportion on emulsion printability. A control sample without ChNC and with an O/W ratio of 6/4 (P_4P_6G) was also prepared for subsequent comparative analysis of rheological and printing properties.

In the Fourier transform infrared (FTIR) spectra (Fig. 2(e)), compared to the hydroxyl absorption peak of PVA at 3335 cm^{-1}, the PCPG exhibited a hydroxyl absorption peak at 3332 cm^{-1}, demonstrating a distinct red shift, which indicates the presence of hydrogen bonding within the system [32]. This shift is attributed to the formation of intermolecular hydrogen bonds between the hydrophilic groups (amino and hydroxyl groups) on the ChNC surface and the hydroxyl groups on the PVA molecular chains. Additionally, compared to the C–H stretching vibration absorption peaks of PW (2914 and 2848 cm^{-1}), the C–H stretching vibration absorption peaks of the multiphase gel (2914 and 2848 cm^{-1}) also exhibited a noticeable red shift. This is induced by hydrophobic interactions between the hydrophobic acetyl groups (–CO–CH_3) on the ChNC surface and the methyl groups (–CH_3) on the phase-change PW molecular chains. Next, the interaction was characterized by X-ray photoelectron spectroscopy (XPS). The high-resolution C 1s spectra (Fig. S11 and Table S1 in the ESM) show that the C–O=C peak in ChNC shifts from 289.10 to 289.29 eV to high binding energy, while the C–O peak of PVA shifts from 286.40 to 286.22 eV to low binding energy after mixing ChNC with PVA. In the O 1s spectrum, the binding energy of C–OH peak in PVA shifted from 532.39 to 532.42 eV, and the binding energy of C=O peak in ChNC shifted from 531.51 to 531.76 eV (Table S2 in the ESM). This indicates that there is a hydrogen bond interaction between ChNC and PVA. In addition, the N 1s peaks of ChNC at –NH–CO– (400.27 eV) and –NH_2 (399.75 eV) moved to 400.49 and 399.77 eV (Table S3 in the ESM), respectively, after mixing with PVA, which further confirmed the formation of hydrogen bonds [33]. X-ray diffraction (XRD) results (Fig. 2(d)) further verified the structural integrity of the system. The XRD pattern displayed characteristic diffraction peaks of ChNC at 2θ = 9.2°, 12.5°, 19.2°, 20.6°, 23.2°, and 26.3°, corresponding to its (020), (021), (110), (120), (130), and (013) crystal planes, respectively; the semi-crystalline characteristic diffraction peaks of PVA were observed at 2θ = 19.6° and 40.8°, corresponding to the (101) and (002) crystal planes of PVA, respectively [32]. In the pattern of the PCPG, the characteristic peaks of all components were preserved, indicating that the crystal structures of the components remained unchanged during the 4D printing forming process.

To investigate the spatial distribution characteristics of ChNC within the multiphase gel, confocal laser scanning microscopy (CLSM) was used to observe ChNC stained with Calcofluor white (1 mg·mL^{-1}, blue) [18]. The results showed that ChNC were uniformly distributed within the gel matrix (Fig. 2(f) and Fig. S6 in the ESM). Combining scanning electron microscopy (SEM) images (Fig. 2(g)) and atomic force microscopy (AFM) images (Fig. 2(h)), it can be clearly observed that ChNC distribute along the oil droplets, resulting in the uniform dispersion of the PW oil phase within the PVA matrix. This effectively ensures the stability of the oil–water interface and provides support for subsequent printability. During the emulsification process, ChNC effectively inhibit the aggregation of oil droplets through steric hindrance, thereby facilitating the formation of a Pickering emulsion with a higher O/W ratio. The increased content of the phase-change material ensures the excellent shape memory properties of the multiphase gel. Molecular dynamics (MD) simulation results revealed the interaction mechanisms at the molecular level within the PCPG system (Figs. 2(i)–2(l)). Figures 2(i) and 2(k) show that

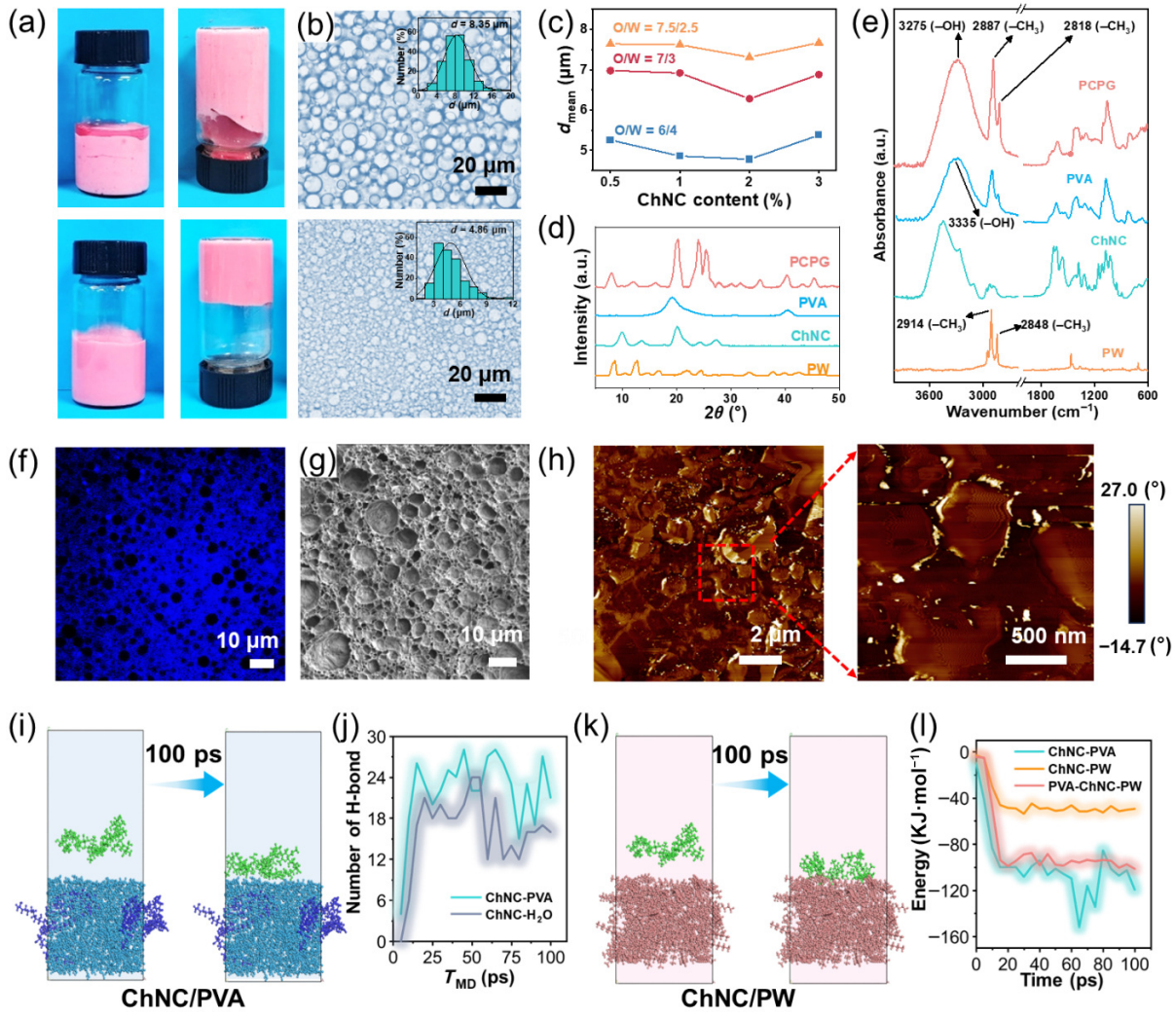

Figure 2 Physical and chemical structural characterization of PCPG. (a) Photographs of Pickering emulsions with O/W = 7.5/2.5 without ChNC (top) and with ChNC (bottom). (b) Optical microscope images and corresponding particle size distribution plots (inset) of Pickering emulsions with O/W = 6/4 at 0 wt.% (top) and 2 wt.% (bottom) ChNC. (c) Particle sizes of Pickering emulsions at different O/W ratios when 0.5 wt.%, 1 wt.%, 2 wt.%, and 3 wt.% ChNC are added. (d) The XRD patterns and (e) FTIR spectra of PCPG, PVA, ChNC, and PW. (f) The CLSM image, (g) SEM image, and (h) AFM images of the PCPG. (i) Representative snapshots of the ChNC-PVA system at different time points. (j) Hydrogen bonding force statistics between ChNC and PVA chains, as well as between ChNC and water. (k) Representative snapshots of the ChNC-PW system at different time points. (l) Changes in the interaction energy about ChNC-PVA, ChNC-PW, and PVA-ChNC-PW.

ChNC rapidly accumulate at the oil–water interface during the simulation time of 100 ps, and ChNC adsorb with PVA and PW, respectively. The number of hydrogen bonds between ChNC and H_2O is less (~ 20), while the number of hydrogen bonds between ChNC and PVA is more (~ 27). The number of hydrogen bonds increased rapidly at 10 ps, resulting in spontaneous adsorption, which was consistent with the previous hypothesis and FTIR analysis. The results of Fig. 2(l) show that there are interactions between ChNC and PVA, ChNC and PW, ChNC and PVA and PW, which can produce spontaneous adsorption. This multiple and strong interaction promotes the formation of nanoconfinement effect, and has far-reaching significance for the mechanical stability and reprocessability of multiphase gels [34, 35] (the models of ChNC, PW, and PVA are shown in Fig. S5 in the ESM. Interaction energy calculation Eq. (S1) in the ESM).

2.2 Printability of PCPG

The introduction of ChNC significantly improved the stability and microstructure of the PVA/PW pickering emulsion, particularly enhancing the oil–water interfacial binding strength and enabling the stable construction of high O/W ratio emulsions. Interfacial stability plays a decisive role in determining the rheological properties of the Pickering emulsion as a 3D printing ink, directly influencing its extrusion fluency, shape fidelity, and structural stability [36]. Therefore, the rheological behavior of the emulsions was systematically investigated. The results indicated that the prepared emulsions exhibited pronounced shear-thinning behavior (Fig. 3(a)), suggesting that the system possesses good fluidity and printability under applied stress. Based on the rheological test data, the thixotropy index of the emulsions was calculated using Eq. (1)

$$\mathrm{IT} = \frac{\eta_{0.1}}{2\eta_1} + \frac{\eta_{0.2}}{2\eta_2} \quad (1)$$

where $\eta_{0.1}$, η_1, $\eta_{0.2}$, and η_2 represent the viscosity of the emulsion at shear rates of 0.1, 1, 0.2, and 2 s^{-1}, respectively. Theoretically, a higher thixotropy index indicates better thixotropic properties of the emulsion, meaning that it can rapidly recover its viscosity after shear thinning during the printing process, which is more

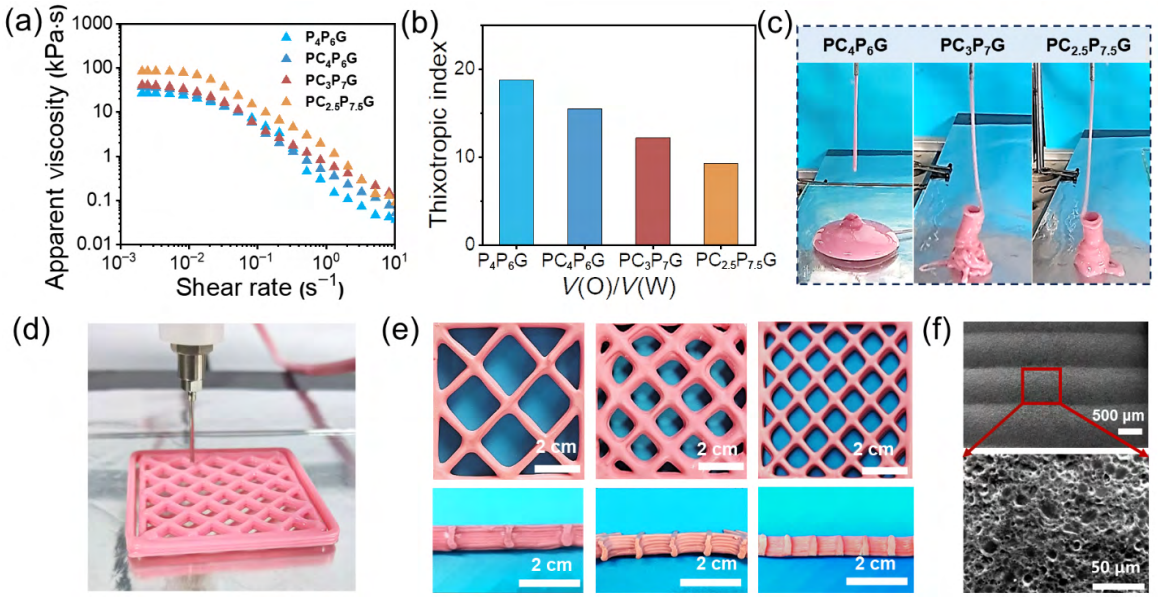

Figure 3 Printability characterization of PCPG. (a) Viscosity versus shear rate, (b) thixotropic index, and (c) photographs of the emulsion extruded through a printing nozzle (nozzle inner diameter of 1.2 mm) for Pickering emulsions and PVA solutions with different O/W ratios. (d) Photograph of the 3D printing process for a cubic scaffold. (e) Photographs of cubic scaffolds with different filling densities, observed from a top view (top) and cross-sectional view (bottom). (f) Cross-sectional view of the cubic scaffold and its surface magnified SEM image.

conducive to 3D printing [37]. According to the calculation results in Fig. 3(b), the emulsion with O/W = 6/4 exhibits a relatively high thixotropy index, theoretically making it more suitable for 3D printing. However, practical printing results (Fig. 3(c)) revealed that although the O/W = 6/4 emulsion rapidly recovers its viscosity after extrusion, its initial viscosity is too low to allow the extruded filament to maintain its shape [24]. In contrast, the emulsions with O/W = 7/3 and 7.5/2.5, possessing sufficiently high initial viscosities, can rapidly set after printing, demonstrating superior printability.

Consequently, the prepared Pickering emulsion can be utilized for 4D printing to address the issue of limited geometric structures in SMGs. Using the high internal phase Pickering emulsion with 2 wt.% ChNC as the emulsifier and O/W = 7.5/2.5 as the printing ink, 4D printing of the shape memory gel was achieved, successfully fabricating cubic scaffolds with infill densities of 10%, 15%, and 20% (Figs. 3(d) and 3(e), and Movie S1 in the ESM). To further enhance the structural stability and mechanical properties of the scaffolds, the printed scaffolds underwent five freeze-thaw cycles (4 °C for 4 h of freezing, and 50 °C for 0.5 h of thawing) to obtain stable multiphase gels. SEM images of the side and cross-sectional views of the multiphase gel scaffolds with different infill densities (Fig. 3(f) and Fig. S7(a) in the ESM) show that the printed scaffolds have layers that are closely stacked and firmly bonded, and exhibit strong interlayer interactions. The phase-change microgels are encapsulated within the continuous gel network, and the particle size of the microgels is consistent with the results from optical microscopy (Fig. S4 in the ESM). The laser focusing microscopy images (Fig. S8 in the ESM) demonstrate that the surface topography of the multiphase gel exhibites a height difference within 30 μm, indicating low roughness and high smoothness. This further confirms the uniform dispersion of PW within the gel matrix. Therefore, these microgel inclusion domains can act as micro-encapsulants within the multiphase gel to provide shape memory properties.

2.3 Shape memory and mechanical properties of PCPG

Due to the phase transition of the microgel inclusions from rigid solid in the fully crystalline state to viscous liquid in the molten state, the multiphase gel exhibits tunable mechanical responses at different temperatures (Fig. 4(a)). Specifically, governed by the phase transition of the PW within the microgel inclusions, PCPG demonstrates a programmable switch mechanism characterized by distinct modulus plateaus (Fig. 4(b)). The storage modulus (G') of the multiphase gel maintains a high plateau (9.5×10^5 Pa) below 35 °C. Notably, as the temperature increases, G' exhibits a sharp and nearly order-of-magnitude decrease (down to 8.5×10^4 Pa) across a specific temperature range of 35–43 °C. Combined with differential scanning calorimetry (DSC) results (Fig. S9 in the ESM), this sharp modulus drop region (Fig. 4(b)) perfectly correlates with the endothermic melting peak range (35–43 °C) of the phase-change PW. Therefore, this drastic decrease in G' is definitively attributed to the reduced crystallinity and the solid-to-liquid phase transition of the microgel inclusions within this specific temperature window [6]. Two modulus plateaus were observed over a wide temperature range (5–35 °C and 43–60 °C), revealing the multi-stable mechanical characteristics of the multiphase gel. This multi-stability enables the material to reversibly switch between a "rigid state (9.5×10^5 Pa)" and a "flexible state (8.5×10^4 Pa)" in response to external temperature stimuli. The multi-modulus switching of PCPG caused by external stimulation can make it of great application value in the field of bionic vascular scaffold and intelligent soft robot [1, 18]. Further tensile tests confirmed this switching mechanism: As shown in Figs. 4(c) and 4(f), the multiphase gel exhibits a "strong yet brittle" character with high modulus, high strength, and low fracture elongation below the PW melting point (T_m) of the phase-change PW, while it transitions to a more flexible state above T_m. Correspondingly, the tensile modulus (E) and fracture strength (σ_b) below T_m are significantly higher than those above T_m (Figs. 4(d), 4(e), 4(g), and 4(h)), while the fracture elongation (ε_b) below T_m is significantly smaller than that above T_m

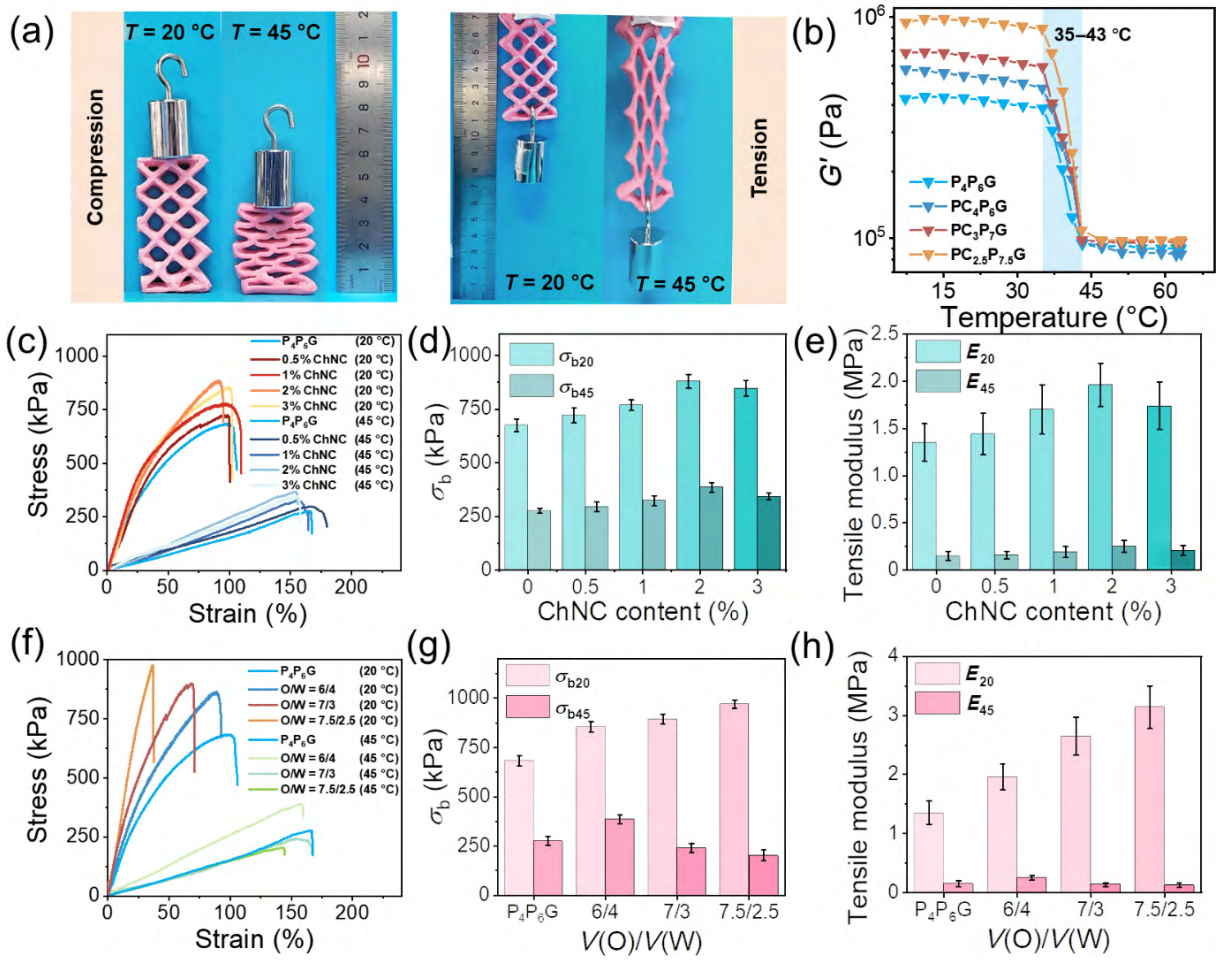

Figure 4 Characterization of the programmable mechanical properties of PCPG. (a) Photographs of the tensile and compressive morphologies of the grid-like multiphase gels under a load of 50 g above and below the PW T_c. (b) DMA test curves of Pickering emulsions with different O/W ratios (frequency: 1 Hz, strain: 0.2%, temperature range: 5–65 °C, and heating rate: 2 °C·min^{-1}). (c) Stress–strain curves, (d) tensile strength, and (e) tensile modulus comparison of organic hydrogels with different ChNC contents (O/W = 6/4) at 20 and 45 °C. ((f)–(h)) Comparison of (f) stress–strain curves, (g) tensile strength, and (h) tensile modulus of multiphase gels containing 2 wt.% ChNC emulsifier at 20 and 45 °C with different O/W.

(Fig. S9 in the ESM). Therefore, through an on-demand modular assembly strategy, the multiphase gel exhibits switchable mechanical properties due to the phase transition of the microgel inclusions. When the multiphase gel undergoes heating–cooling cycles (20 ↔ 45 °C), the modulus can reversibly switch between the two stable states due to the inherent crystallization-melting characteristics of the oleophilic component, with good cycling stability. Consequently, precisely controllable multi-stable mechanical properties can be achieved in the complex multiphase gel, enabling programmability of the multiphase gel material [6].

Furthermore, Fig. 4(c) also shows the effect of different ChNC mass fractions on the tensile properties of the multiphase gel. The results show that the σ_b and E of the multiphase gel gradually increase with higher ChNC content, while ε_b shows little change (155%–160%) (Figs. 4(d) and 4(e), and Fig. S10 in the ESM). When the ChNC content are 2 wt.%, the σ_b and E of the gel reach maximum values (880 kPa and 1.96 Mpa, respectively), which is also consistent with the previous analysis of oil droplet distribution and particle size statistics. This enhancement effect can be attributed to the stable interfacial interactions formed between ChNC and the oil/water phases (Figs. 2(d) and 2(h)), effectively improving the mechanical properties of the gel. However, further increasing the ChNC content leads to a decline in the mechanical performance of the gel. This is because chitin molecules possess a high density of intermolecular hydrogen bonds. Although some hydrogen bonds are broken after the deep eutectic solvent (DES) reaction, a majority are retained. When the ChNC concentration reach a certain level, this leads to the nanocrystals approaching each other and aggregating due to hydrogen bonding [20]. This aggregation behavior weakens the stabilizing effect of ChNC at the oil–water interface, reducing the interfacial enhancement effect and consequently decreasing the mechanical properties of the gel. Overall, an appropriate amount of ChNC (2 wt.%) significantly enhance the mechanical properties of the multiphase gel, ensuring high structural stability and programmable 4D printing performance.

Figure 4(f) displays the effect of varying oil phase content on the mechanical properties of the multiphase gel (using 2 wt.% ChNC as the emulsifier). The results indicate that as the oil phase content increases, the ε_b (96%–36%) and E (1.35–3.14 MPa) of the multiphase gel show a decreasing trend; when the temperature is above T_m, σ_b (276–203 kPa) also decreases (Figs. 4(f)–4(h) and Fig. S11 in the ESM). This is because the increased oil phase content raises the proportion of weak oil–water interfaces within the gel,

leading to the decline in mechanical performance. Conversely, when the temperature is below T_m, the σ_b of the gel increases with higher oil phase content, as the PW is in a crystalline state at this point, and these crystalline phases effectively enhance the rigidity and strength of the gel. In summary, the synergistic regulation of ChNC content and oil phase ratio significantly influences the mechanical properties of the multiphase gel, providing an important basis for optimizing the structural stability and reversible deformation characteristics of its 4D-printed constructs.

2.4 Shape memory principle and programmability of PCPG

The synergistic combination of the phase-change microgels and the stable gel scaffold constructs a multiphase gel with shape memory characteristics (Figs. 5(a) and 5(b)). Above T_m, the phase-change PW is in a liquid state, softening the microgel domains and endowing the wet material with plasticity and processability, allowing it to be deformed into a temporary shape under external force. When the material is cooled below the crystallization temperature (T_{crys}) of the PW, the crystalline phase-change PW contributes to fixing the temporary shape of the multiphase gel. Subsequently, simply heating the material above T_m causes the crystalline PW to melt again, and the release of stored energy drives the network rebound, allowing recovery to its original shape (Figs. 5(c) and 5(e)). This demonstrates the shape memory behavior of the multiphase gel, indicating its ability to fix a temporary shape or recover its original shape via thermal stimulation. To more specifically characterize the shape memory properties of multiphase gels with different O/W ratios (Fig. S12(a) in the ESM), we stretched the working region of the gel by 100% after raising the temperature above T_m (45 °C), cooled it in 20 °C water to fix the shape, and calculated the material's shape fixed ratio (R_f) using Eq. (2)

$$R_f = \frac{L_t - L_0}{L_s - L_0} \times 100\% \quad (2)$$

where L_0, L_t, and L_s represent the original length, temporary length, and stretched length, respectively [32].

Subsequently, the fixed-shape gel is reheated above the T_m of the PW to recover its shape, and the shape recovery ratio (R_r) of the material is calculated using Eq. (3)

$$R_r = \frac{L_t - L_r}{L_t - L_0} \times 100\% \quad (3)$$

where L_0, L_t, and L_s represent the original length, temporary length, and recovered length after shape recovery, respectively [32].

The calculation results (Fig. S12(b) in the ESM) show that as the oil phase content increases, the R_f and R_r of the multiphase gel are significantly enhanced, indicating that the proportion of the phase-change component plays a key regulatory role in the shape memory

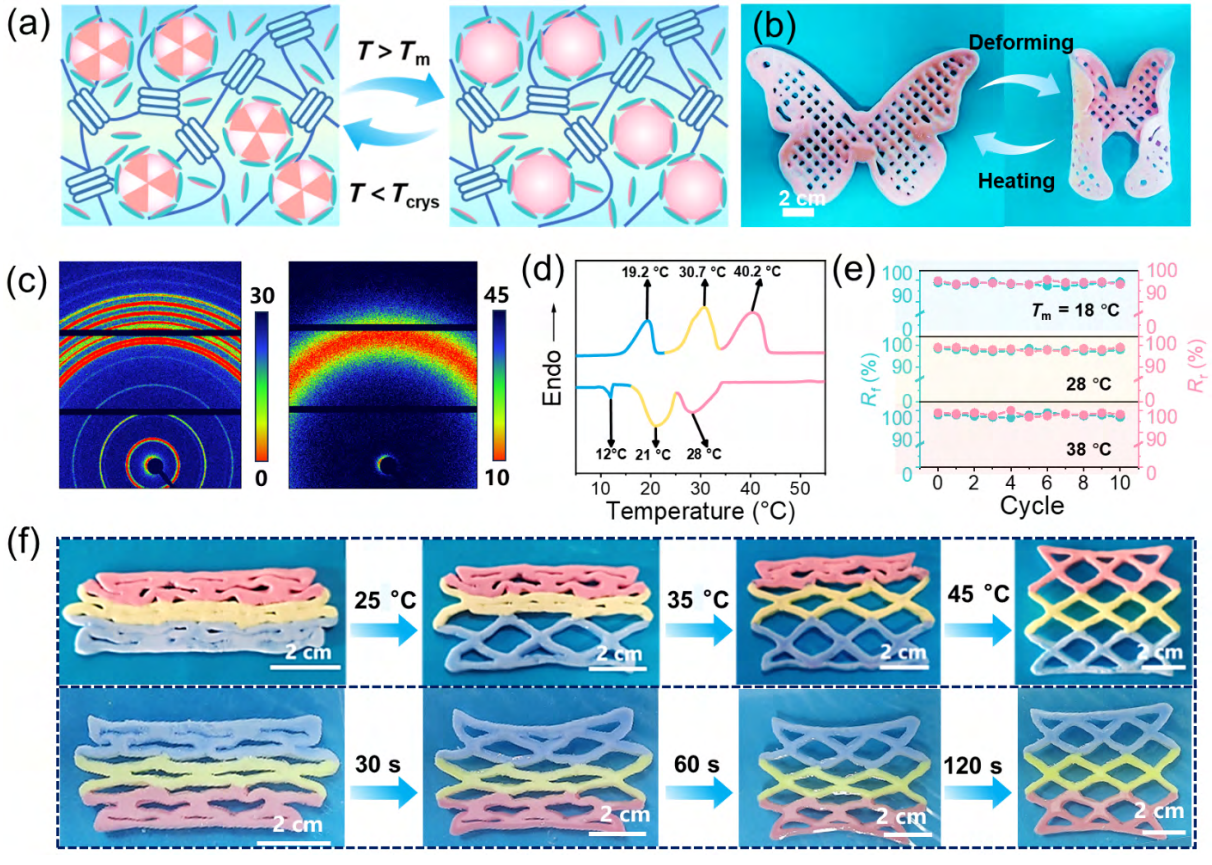

Figure 5 Shape memory principle and characterization of 4D-printed PCPG. (a) Schematic diagram of the shape memory mechanism of the multiphase gel based on the phase transition of PW: The solid–liquid phase transition of PW microdroplets in the dispersed phase is controlled by temperature changes. (b) Demonstration of the shape memory process of 4D-printed multiphase gels. (c) Wide-angle X-ray scattering (WAXS) patterns of the multiphase gel under conditions below T_m (20 °C, left) and above T_m (45 °C, right). (d) PW with different T_m values serves as the emulsion oil phase. DSC curves of segmentally printed multiphase gel scaffolds. (e) Cyclic shape memory performance of multiphase gels with an O/W ratio of 7.5/2.5 (change in R_f rate and R_r rate with the number of cycles). (f) Demonstration of the shape memory process of multiphase gel scaffolds printed in segments using PW with different T_m as the oil phase.

properties. By using PW with different T_m on a single spline and gradually increasing the temperature, the multiphase gel progressively recovers its original shape, demonstrating its multifunctional intelligent responsiveness (Fig. S12(c) in the ESM). Cyclic shape memory performance tests (Fig. 5(e) and Fig. S13 in the ESM) further revealed that the R_f and R_r of the multiphase gel remain stable after several heating-cooling cycles, demonstrating excellent shape memory stability. The multiphase gel with O/W = 7.5/2.5 maintained both R_f and R_r above 97%, exhibiting efficient and repeatable thermally responsive memory capability. Furthermore, based on the test results from Figs. 4(f)–4(h) and Fig. S11 in the ESM, the mechanical properties of the multiphase gels prepared from the printable emulsions with O/W = 7/3 and O/W = 7.5/2.5 show little difference. Therefore, for subsequent experiments, the Pickering emulsion prepared with 2 wt.% ChNC as the emulsifier and O/W = 7.5/2.5 was selected as the ink for extrusion-based 4D printing of the multiphase gel.

After determining the parameters for the ink used in extrusion-based 4D printing, a butterfly model was printed (Movie S2 in the ESM), and its shape memory process, along with that of the printed scaffold, was demonstrated (Fig. 5(b) and Movie S3 in the ESM). The results show that the 4D-printed model exhibits excellent R_f, effectively resolving the difficulty of forming complex geometric structures with gels. Furthermore, the model can almost completely recover its original shape after deformation, demonstrating outstanding shape memory properties. The emulsions prepared by phase change PW with phase change temperatures (T_m) of 18, 28, and 38 °C were used as inks (Figs. S3(c) and S3(d) in the ESM). A multiphase gel scaffold was constructed by segmented printing (SEM images of the interface between gels with different phase transition temperatures (T_c) are shown in Fig. S7(c) in the ESM. The interfacial strength is shown in Fig. S7(d) in the ESM. Figure 5(d) shows the DSC analysis results of the multiphase gel composed of PW oil phases with different T_m. The data showed that the melting points of PW increased to 19.2, 30.7, and 40.2 °C, respectively. This change can be attributed to the nano-confinement effect of ChNC, which effectively suppresses the thermal motion of PW molecular chains, thus requiring higher thermal energy to overcome the phase transition energy barrier [38, 39]. Upon gradually heating the compressed multiphase gel scaffold, the different PWs underwent sequential phase transitions, causing the scaffold to recover its original shape in stages (Figs. 5(e) and 5(f)). This result indicates that PWs with different T_m values can be used to program 4D-printed multiphase gel models, enabling precise control where different parts of the model recover their shape at specific required temperatures, further demonstrating the excellent programmability of our prepared multiphase gel.

With the rapid development of biomedical engineering, the application of biological scaffolds in the fields of tissue engineering, drug delivery, and regenerative medicine is becoming increasingly widespread [15, 40, 41]. Compared to traditional solid shape memory polymers, SMGs possessing a three-dimensional network structure and high water content exhibit excellent mechanical elasticity, biocompatibility, flexibility, and environmental responsiveness, making them ideal materials for biological scaffolds. A phase-change PW with a transition temperature close to human body temperature (38 °C) was selected to program the 4D-printed vascular stent. After fixing the vascular stent into a temporary shape and implanting it into the blood vessel, the phase-change PW in the stent melted within 1 min, causing the stent to automatically expand (Fig. 6(a) and Movie S4 in the ESM). Furthermore, ChNC can improve the mechanical properties of the multiphase gel to a certain extent (Fig. 4(c)), enabling it to function as a vascular support.

Additionally, since the triggering condition for traditional shape memory materials is typically thermal, primarily based on the glass transition of polymers or the melting of crystals as the switching mechanism, and considering the design of devices intended to change shape after placement in vivo, we aimed to trigger shape recovery in a non-invasive manner. This involves concentrating thermal energy on the biomaterial and applying it briefly to avoid thermal damage to surrounding tissues, thereby minimizing associated medical risks [42]. As shown in Fig. 6(b), high intensity focused ultrasound (HIFU) was selected as the method for remote energy input to achieve non-invasive heating and shape activation of the implantable 4D-printed stent. Ultrasound energy can be precisely targeted to the material located beneath multiple tissue layers via mechanical waves or acoustic radiation effects, offering advantages such as high safety, controllability, and localized heating efficiency [43]. Further verification was conducted to determine whether the 4D-printed vascular stent possesses ultrasound responsiveness. The verification results (Fig. 6(c) and Movie S5 in the ESM) indicate that the multiphase gel is indeed responsive to ultrasound. Part of the energy generated during the ultrasound process is absorbed by the gel matrix and the phase-change microgels. This absorption leads to the melting of crystalline regions within the microgels and the disruption of reversible hydrogen bonds in the gel matrix, consequently inducing shape recovery in the multiphase gel. Moreover, it can be programmed using PW with different T_m values, making its shape recovery controllable, which significantly broadens the application scope of vascular stents. Benefiting from our natural ChNC raw materials and chemical components with good biocompatibility, cell culture experimental results (Figs. 6(d) and 6(e)) show that the cell survival rate in the culture dish containing the multiphase gel is similar to that of naturally growing cells, indicating that the prepared multiphase gel possesses good biocompatibility.

2.5 Reprocessable of PCPG

The stability of the multiphase gel's precursor, the Pickering emulsion, originates from the adsorption of amphiphilic solid particles. These particles adsorb dynamically at the oil–water interface, forming a stable emulsion structure. Unlike traditional emulsifiers, these particles are not consumed or degraded like surfactants, thus retaining their functionality even after emulsion breakdown or separation, enabling reversible emulsification after the emulsion structure is disrupted [44, 45]. Furthermore, the gel matrix of the multiphase gel is formed through dynamically and physical crosslinking between PVA molecular chains. This physically crosslinked structure can be disrupted under heating, allowing the PVA chains to redisperse in the aqueous phase, thereby achieving the dissolvability and reconfigurability of the multiphase gel and enabling recycling [46]. Consequently, the re-emulsifiable characteristics of the Pickering emulsion combined with the reversible physical crosslinking of the PVA matrix make the reprocessability of the multiphase gel possible.

Figure 7(a) illustrates the recycling process of the 4D-printed multiphase gel: The printed PCPG scaffold is cut into pieces and redissolved, disrupting the emulsion structure and separating the oil and water phases. Subsequently, stable emulsion can be reobtained

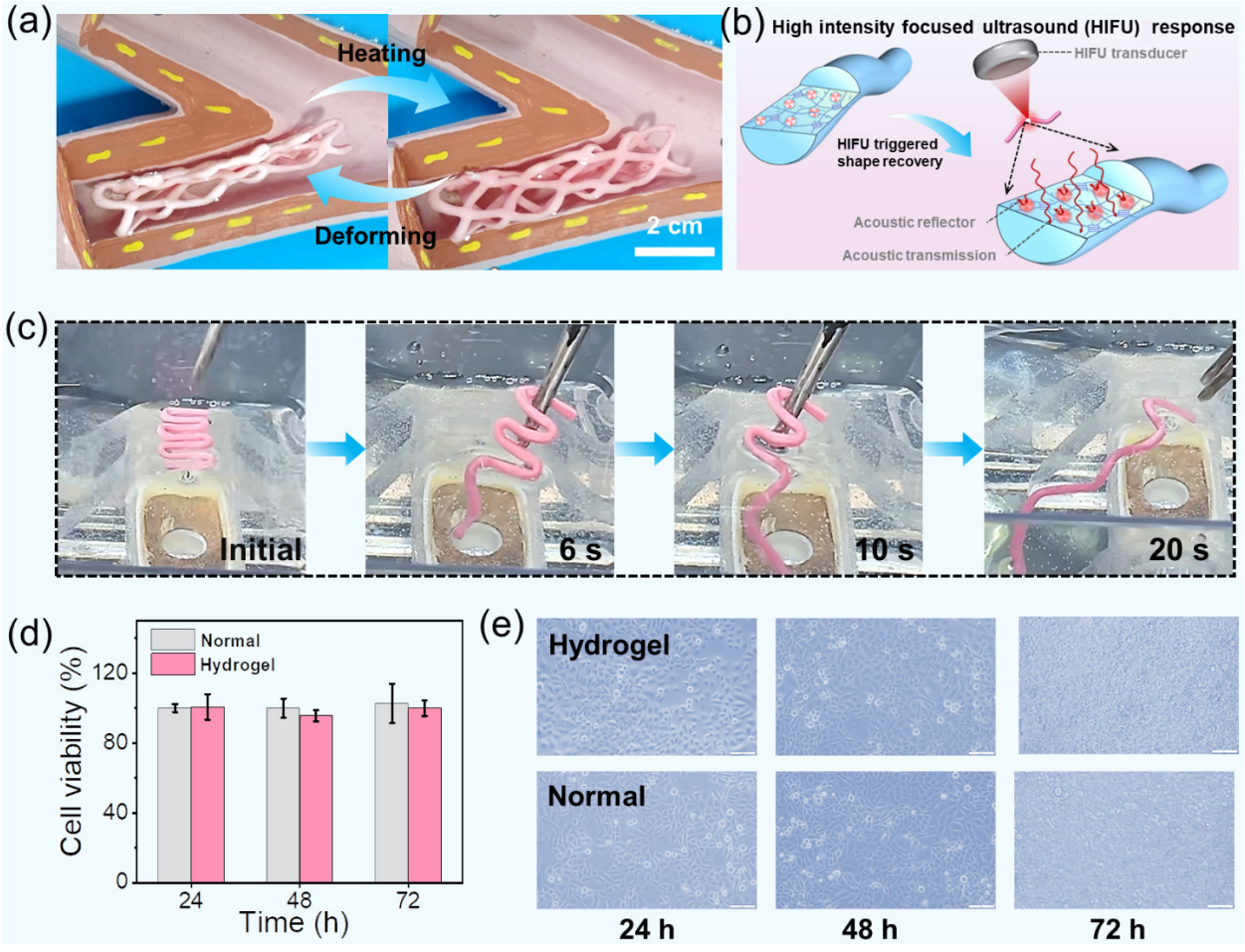

Figure 6 Application demonstration of 4D-printed multiphase gel scaffolds. (a) Thermal response-induced shape regulation: heating-deformation cycle process simulated in a vascular environment. (b) Schematic of PW phase transition behavior triggered by HIFU remote heating in multiphase gel network structures. (c) Ultrasound-driven deformation: Simulating the dynamic deformation cycle of a vascular stent. (d) Cell viability at different time points after putting in multiphase gel. (e) Cell culture images of multiphase gel and control group (24, 48, and 72 h).

through re-emulsification, and finally, the multiphase gel can be refabricated via 4D printing and freeze-thaw cycles. The schematic diagram in Fig. 7(b) further elucidates the recycling mechanism: Heating induces the disruption of physical crosslinks within the gel network, dissociating the PVA crosslinked network into individual PVA chains; during subsequent freeze-thaw cycles, physical crosslinks between PVA chains reform, constructing a new gel network and yielding the multiphase gel. Figure 7(e) shows that the shape memory properties of the multiphase gel slightly decrease (by 5%) after recycling but still remain excellent (R_f and R_r > 90%). Simultaneously, DSC analysis (Fig. S15 in the ESM) indicates that after ten recycling cycles, the T_m and T_{crys} of the phase-change microgels remain stable, and their crystal structure shows no significant changes (Fig. S16 in the ESM), demonstrating the good structural stability and programmability of the multiphase gel. Additionally, its σ_b and ε_b change only slightly both above and below T_m (Figs. 7(c), 7(d), 7(f), and 7(g), and Fig. S14 in the ESM), further indicating the stable programmable mechanical performance of the multiphase gel and confirming the stability of its programmability. Therefore, the multiphase gel exhibits excellent reprocessability. Based on the stable programmability, mechanical properties, and shape memory performance maintained after multiple recycling cycles, it provides a new pathway for the re-processing and functional printing of fabricated gels, significantly enhancing the material's potential value in sustainable intelligent manufacturing and regenerative applications.

3 Conclusions

In summary, this work presents a 4D printing strategy based on Pickering emulsions for constructing programmable and reprocessable multiphase gels. By introducing amphiphilic ChNC as a solid emulsifier, a stable PVA/PW Pickering emulsion system was constructed. The interactions between the ChNC, PVA gel matrix, and phase-change PW improved the oil–water interfacial strength, thereby significantly enhancing the mechanical properties of the multiphase gel (600 → 900 kPa). Simultaneously, the steric hindrance effect of ChNC enabled the controlled construction of a high internal phase emulsion (oil phase volume fraction of 75%), endowing the multiphase gel with excellent shape memory properties (R_f and R_r > 95%). Relying on the excellent shear-thinning behavior of the Pickering emulsion and the high initial viscosity (> 75 kPa·s) characteristic of the high internal phase emulsion, its feasibility as an ink for extrusion-based 4D printing was achieved, solving the problem of limited formable geometries for gels. The mechanically programmable multiphase gel enables thermally responsive property switching and application-specific performance tuning in biological scaffolds, while also being

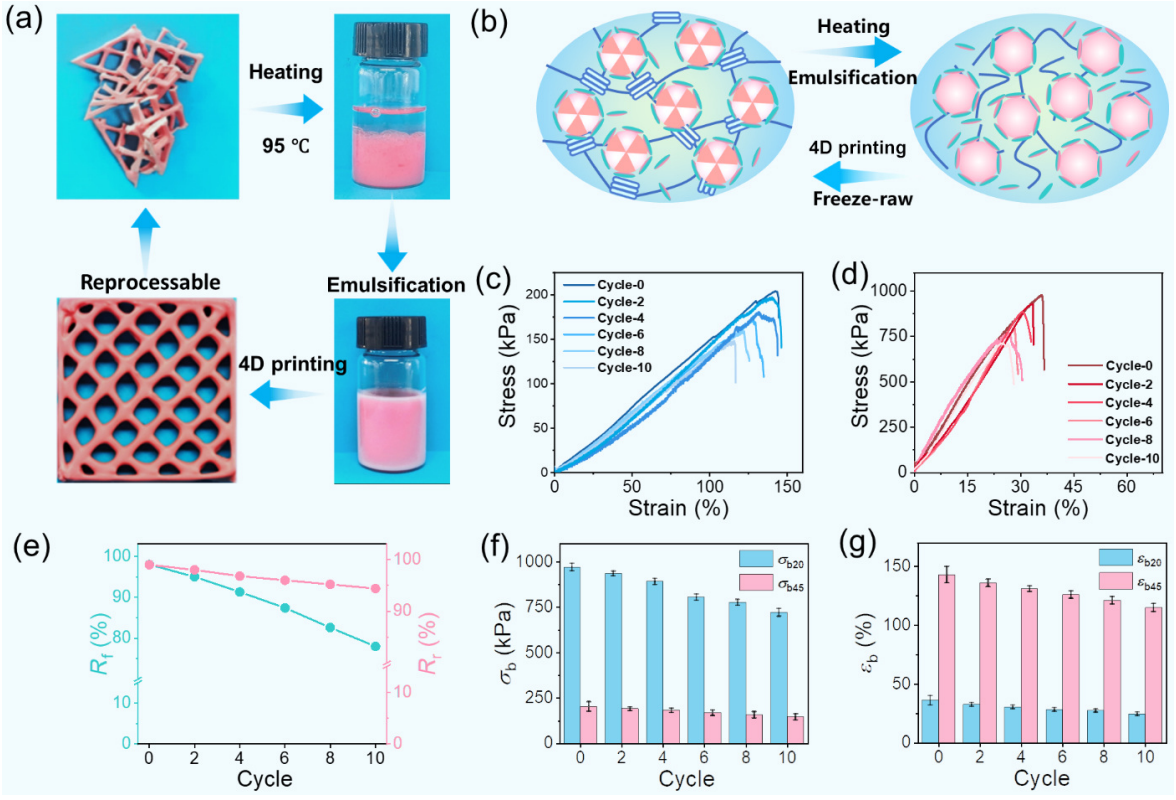

Figure 7 Characterization of the reprocessability of 4D-printed PCPG. (a) Schematic diagram of the recycling process. (b) Microstructural mechanism of reprocessability. (c) Stress–strain curves of samples with different recycling cycles at temperatures above T_m. (d) Stress–strain curves of samples with different recycling cycles at temperatures below T_m. (e) Shape memory performance (R_f/R_f) as a function of recycling cycles. (f) Fracture strength and (g) fracture elongation as a function of recycling cycles, with statistical comparisons.

reprocessable. This multiphase gel, with its excellent shape memory, programmable geometries and mechanical properties, and reprocessability, opens new avenues for the application of biological scaffolds in biomedical engineering.

4 Experimental

4.1 Materials

PVA 1799 was provided by Kuraray China Co., Ltd. Chitin was purchased from Zhejiang Golden-Shell Pharmaceutical Co., Ltd. Choline chloride (ChCl) and oxalic acid (OA) were purchased from Saan Chemical Technology (Shanghai) Co., Ltd. p-Toluene sulfonic acid (p-TsOH) was purchased from Shandong Keyuan Pharmaceutical Co., Ltd. Sodium hydroxide (NaOH), hydrochloric acid (HCl), dimethyl sulfoxide (DMSO), and 3-(4,5-dimethyl-2-thiazolyl)-2,5-diphenyl tetrazolium bromide (MTT) were purchased from Sinopharm Chemical Reagent Beijing Co., Ltd. PW (T_m = 18, 28, and 38 °C) was purchased from Guangzhou Zhongjia New Materials Technology Co., Ltd. Nanoclay was purchased from Jiangsu XFNANO Materials Technology Co., Ltd. Oil colour (Mary Brand O-1050) was purchased from Shanghai Mary Painting Materials Co., Ltd. Fluorescent whitening agent was purchased from Shanghai Sigma Co., Ltd. CNF, ChNF, and CNC were prepared by the preparation method of the research group. Intestinal epithelial cell (NCM460) was purchased from Shanghai yuanye Bio-Technology Co., Ltd. All the chemicals were used as purchased without further purification.

4.2 Preparation of amphiphilic ChNC

ChNC were prepared by DES method. DES was prepared by mixing ChCl, p-TsOH acid, and OA at a molar ratio of 2:1:1 to form a 150 g mixture, which was stirred at 80 °C for 30 min. 3 g of chitin was added to the DES and stirred at 80 °C for 4 h. The reaction mixture was centrifuged at 8000 r·min^{-1} for 5 min. The lower precipitate was collected, while the upper DES supernatant was recovered for reuse. The precipitate was dialyzed against deionized water until the conductivity was below 200 μS·cm^{-1}. The resulting sample was subjected to ultrasonication for 10 min using an ultrasonic cell disruptor to obtain an aqueous dispersion of ChNC. Different concentrations (0.5 wt.%, 1 wt.%, 2 wt.%, and 3 wt.%) of ChNC dispersions were prepared via rotary evaporation.

4.3 Preparation of the high internal phase Pickering emulsion

60 g of PVA powder was added into 240 mL of deionized water and stirred at 95 °C for 6 h. 20 mL of PVA solution, 20 mL of ChNC aqueous dispersion, and 60 mL of PW (volume ratio O/W = 6/4) were stirred at 8000 r·min^{-1} for 5 min by a high-speed shear emulsification machine to form a stable oil-in-water Pickering emulsion. High internal phase Pickering emulsions with O/W = 7/3 and 7.5/2.5 were prepared by the same method.

4.4 Preparation of multiphase gels (PCPG)

The prepared emulsion was printed according to the programming model by an extrusion 3D printer. After printing, the PCPG was obtained by five freeze-thaw cycles (freezing at ~ 4 °C for 4 h and

melting at ~ 35 °C for 30 min). Preparation method of multiphase gel scaffolds: Emulsions with different phase transition temperatures (containing paraffin with different phase transition temperatures) were printed separately, and the two scaffolds were bonded together using the prepared emulsion as an adhesive. Subsequently, freeze-thaw cycles were performed as described above.

4.5 MD simulations

All simulations were performed using Materials Studio software under the COMPASS force field. Modeling: The chitin molecule minimized the energy of the initial molecular structure through the Forice module. The Amorphous Cell module was used to construct a water + water + PVA + PW cell, in which the water and PVA cell were constructed according to the mass ratio, and the PW cell was constructed according to the experimental density. The Build Layers function was used to obtain the final simulated unit cell of 40 Å × 40 Å × 80 Å. Adsorption simulation: Molecular dynamics simulations were performed using the Forcite module under periodic boundary conditions, in which the chitin skeleton was constrained while the water, water/PVA, and PW simulation cells were kept rigid. The simulation ran at a canonical ensemble (NVT) constant temperature of 298 K, using a time step of 1 fs and a simulation time of 100 ps to achieve an equilibrium state. At equilibrium, the dynamic trajectory was recorded every 20 ps, 20 frames were provided for hydrogen bond statistics, and the last frame was selected for the calculation of interaction energy.

4.6 Thermo-responsive shape memory process

PCPG was stretched in 45 °C water and then placed in 4 °C water for cooling, and the shape of gel was fixed due to PW phase change crystallization. The shape-fixed gel was placed in 45 °C water again and the deformation was recovered.

4.7 HIFU

Response shape memory process: HIFU equipment was built by ourselves. RIGOL DG4102 function arbitrary waveform generator (Puyuan Jingdian), RSK-K broadband RF power supply (Changzhou RuiSiJieElectronic Technology Co., Ltd.), and self-made ultrasonic focusing probe were used. The ultrasonic focusing probe was placed in a water bath, and the ultrasonic probe could focus the sound wave at a point through the groove (3 cm away from the groove). The gel samples with fixed shape in a 4 °C water bath were placed in a PVA solution (3 wt.%, 20 °C) for ultrasonic response experiments. The shape of the gel was fixed due to PW phase change crystallization. The gel could convert the absorbed ultrasonic sound energy into heat energy. Under the action of ultrasound, the multiphase gel temperature increased, the PW crystal melted, and the shape recovered.

4.8 Biocompatibility characterization

The cytotoxicity of the multiphase gel to NCM460 cells was evaluated using a standard MTT method. NCM460 cells were seeded in 96-well plates at a density of 4000 cells per well. After 24 h of culture, PCPG gel was added for co-incubation for 24, 48, and 72 h, and 100 μL of MTT (0.5 mg·mL^{-1}) was added to each well. The MTT solution was then discarded, and 150 μL of DMSO was added to each well and shaken for 20 min. The absorbance was measured at 490 nm to calculate cell viability. The normal growth of NCM460 cells was used as the control group, and each experiment was repeated three times.

4.9 Reprocessing steps of PCPG

The obtained shape memory hydrogel was cut into small pieces and heated at 95 °C for 4 h to disrupt the hydrogel network, resulting in a mixture with separated oil and water phases. The mixture was then emulsified using the same emulsification method to regenerate the Pickering emulsion. After homogenization of the emulsion, the reprocessed hydrogel could be obtained through extrusion 4D printing and freeze-thaw cycles.

4.10 Characterization

SEM was performed on JSM-7500F at the accelerating voltage of 10 kV. The gel sample was prepared by liquid nitrogen brittle fracture after freeze-drying. XRD measurement was performed on an Ultima IV (Rigaku) with a scanning rate of 5 °·min^{-1}. FTIR spectra of gels samples were obtained using a Bruker VERTEX 70 spectrometer at the range of 4000–500 cm^{-1} and resolutions of 4 cm^{-1}. XPS spectra were recorded on an ESCALAB 250Xi (Thermo Scientiffc) X-ray photoelectron spectrometer, using monochromatic Al Kα (1486.6 eV) radiation as the excitation source. Dynamic rheological measurement was performed on an Ares G2 (TA). Two-dimensional small-angle X-ray scattering (2D SAXS) and two-dimensional wide-angle X-ray diffraction (2D WAXD) spectra were collected using a small-angle/wide-angle X-ray tester (Xenus2.0 SA, France) equipped with a GeniX3D beam transmission system and an anode copper target (Cu Kα). The X-ray wavelength λ was 1.542 Å, and the scattering and diffraction data were analyzed using Fit2D software. Using the Dimension Icon AFM from Bruker, the sample was studied. The testing mode of ChNC water dispersion was Scanasyst. The test mode of the gel sample after ultra-thin section was Tapping. All the tensile tests were executed on an Instron (Micro Tester, 5940) in strain control mode with a strain of 5% per second. The three-dimensional surface structures were tested by laser focusing microscope (KC-X3000, KathMatic). Polarizing microscopy (POM) pictures were obtained by an Olympus BX51 optical microscope. The particle size of oil droplets was calculated by ImageJ software. DSC was tested using a Q20 (TA Instrument) at a heating and cooling rate of 5 °C·min^{-1}. Dynamic mechanical analysis (DMA) was tested using Q800 (TA instrument) at a heating rate of 2 °C·min^{-1}. The test temperature range was 5–65 °C, the frequency was 1 Hz, and the strain was 0.2%. The zeta potentials of the ChNC were determined with a Malvern Nano ZS90 light scattering instrument. 2.5 mL of ChNC suspensions at a concentration of 0.01 mg·mL^{-1} were carried out in triplicate at 25 °C. Laser confocal images were obtained using a Japanese FluoView FV1000 confocal laser scanning microscope with a 355 nm laser source.

Electronic Supplementary Material: Supplementary material (ChNC preparation method, optical images, SEM images, TEM images, intermolecular adsorption energy calculation, DSC curve, XPS curve, mechanical properties curve, and shape memory properties of different oil-water ratios; mechanical curves, DSC curves and XRD patterns after reprocessing; Movie S1: 20% infill cube printing process, Movie S2: 3D printing process for butterfly models, Movie S3: demonstration of shape memory properties in PCPG stents, Movie S4: demonstration of thermal response shape memory properties in 3D-printed vascular stents, and Movie S5: remote-triggered shape recovery of HIFU-induced shape-memory gels) is available in the online version of this article at https://doi.org/10.26599/NR.2026.94908644.

Data availability

All data needed to support the conclusions in the paper are presented in the manuscript and the Electronic Supplementary Material. Additional data related to this paper may be requested fromthecorrespondingauthorupon request.

Acknowledgements

The National Natural Science Foundation of China (Nos. 52573114 and 51903134), Youth Innovation Team Project of Shandong Province, China (No. 2023KJ311), Natural Science Foundation of Shandong Province (No. ZR2024QB049), and China Postdoctoral Science Foundation funded project (No. 2023M732976) are kindly acknowledged for financial support.

Declaration of competing interest

All the contributing authors report no conflict of interests in this work.

Author contribution statement

Z. W. L.: Methodology, data curation, writing – review & editing, writing – original draft, validation, formal analysis. Y. Z. C.: Methodology, data curation, writing – review & editing, writing – original draft, validation, formal analysis. S. H. Z.: Investigation, data curation. Z. S. L.: Software. M. L. Z.: Investigation. S. X. W.: Supervision. Y. X. D.: Supervision, resources. J. M. Z.: Resources, supervision. L. Z.: Conceptualization, writing – review & editing, funding acquisition. All the authors have approved the final manuscript.

Use of AI statement

None.

References

[1] Ni, C. J.; Chen, D.; Yin, Y.; Wen, X.; Chen, X. L.; Yang, C.; Chen, G. C.; Sun, Z.; Wen, J. H.; Jiao, Y. R. et al. Shape memory polymer with programmable recovery onset. *Nature* **2023**, *622*, 748–753.

[2] Yue, T. Q.; Lu, C. H.; Tang, K. L.; Qi, Q. K.; Lu, Z. Y.; Lee, L. Y.; Bloomfield-Gadêlha, H.; Rossiter, J. Embodying soft robots with octopus-inspired hierarchical suction intelligence. *Sci. Robot.* **2025**, *10*, eadr4264.

[3] Li, Z. L.; Wei, S. X.; Théato, P.; Chen, T.; Lu, W. Bioinspired color-changing polymeric hydrogel actuators/robots. *Adv. Mater.* **2026**, *38*, e19281.

[4] Osada, Y.; Matsuda, A. Shape memory in hydrogels. *Nature* **1995**, *376*, 219.

[5] Zhuo, S. Y.; Song, C.; Rong, Q. F.; Zhao, T. Y.; Liu, M. J. Shape and stiffness memory ionogels with programmable pressure-resistance response. *Nat. Commun.* **2022**, *13*, 1743.

[6] Zhuo, S. Y.; Zhao, Z. G.; Xie, Z. X.; Hao, Y. F.; Xu, Y. C.; Zhao, T. Y.; Li, H. J.; Knubben, E. M.; Wen, L.; Jiang, L. et al. Complex multiphase organohydrogels with programmable mechanics toward adaptive soft-matter machines. *Sci. Adv.* **2020**, *6*, eaax1464.

[7] Zhao, Z. G.; Liu, Y. X.; Zhang, K. J.; Zhuo, S. Y.; Fang, R. C.; Zhang, J. Q.; Jiang, L.; Liu, M. J. Biphasic synergistic gel materials with switchable mechanics and self-healing capacity. *Angew. Chem., Int. Ed.* **2017**, *56*, 13464–13469.

[8] Huang, J. C.; Qiu, L. T.; Ni, C. J.; Chen, G. C.; Zhao, Q. Shape memory polymers with patternable recovery onset regulated by light. *Adv. Mater.* **2024**, *36*, 2408324.

[9] Zhang, Y. C.; Hu, Q. Q.; Yang, S. R.; Wang, T.; Sun, W. X.; Tong, Z. Unique self-reinforcing and rapid self-healing polyampholyte hydrogels with a pH-induced shape memory effect. *Macromolecules* **2021**, *54*, 5218–5228.

[10] Cui, Y. D.; Lin, J. H.; Zhai, Y. D.; Xu, C.; Chen, C. J.; Chang, C. Y. Hydration programmable, shape memorable artificial muscles for antagonistic movements. *Adv. Funct. Mater.* **2024**, *34*, 2401005.

[11] Yang, M. J.; Xu, Y. J.; Xin, X. Z.; Zeng, C. J.; Li, Y. S.; Lin, C.; Liu, Y. J.; Guo, Y. Y.; Leng, J. S. 4D printed cardiac occlusion device with efficient anticoagulation, proendothelialization, and precise localization. *Adv. Funct. Mater.* **2025**, 2412533.

[12] Sydney Gladman, A.; Matsumoto, E. A.; Nuzzo, R. G.; Mahadevan, L.; Lewis, J. A. Biomimetic 4D printing. *Nat. Mater.* **2016**, *15*, 413–418.

[13] Puza, F.; Lienkamp, K. 3D printing of polymer hydrogels—From basic techniques to programmable actuation. *Adv. Funct. Mater.* **2022**, *32*, 2205345.

[14] Yu, Z. Y.; Sun, X.; Zhu, Y. L.; Zhou, E.; Cheng, C. F.; Zhu, J. Y.; Yang, P.; Zheng, D. Y.; Zhang, Y. F.; Panahi-Sarmad, M. et al. Direct ink writing 3D printing elastomeric polyurethane aided by cellulose nanofibrils. *ACS Nano* **2024**, *18*, 28142–28153.

[15] Nouseen, S.; Pumera, M. Mxene 3D/4D printing: Ink formulation and electrochemical energy storage applications. *Adv. Funct. Mater.* **2025**, *35*, 2421987.

[16] Lin, Z. W.; Qiu, X. W.; Cai, Z. Q. S.; Li, J. L.; Zhao, Y. N.; Lin, X. P.; Zhang, J. M.; Hu, X. L.; Bai, H. High internal phase emulsions gel ink for direct-ink-writing 3D printing of liquid metal. *Nat. Commun.* **2024**, *15*, 4806.

[17] Zhao, Z. G.; Zhuo, S. Y.; Fang, R. C.; Zhang, L. H.; Zhou, X. T.; Xu, Y. C.; Zhang, J. Q.; Dong, Z. C.; Jiang, L.; Liu, M. J. Dual-programmable shape-morphing and self-healing organohydrogels through orthogonal supramolecular heteronetworks. *Adv. Mater.* **2018**, *30*, 1804435.

[18] Zhao, Z. G.; Zhang, K. J.; Liu, Y. X.; Zhou, J. J.; Liu, M. J. Highly stretchable, shape memory organohydrogels using phase-transition microinclusions. *Adv. Mater.* **2017**, *29*, 1701695.

[19] Zhao, Z. G.; Li, C. X.; Dong, Z. C.; Yang, Y. C.; Zhang, L. H.; Zhuo, S. Y.; Zhou, X. T.; Xu, Y. C.; Jiang, L.; Liu, M. J. Adaptive superamphiphilic organohydrogels with reconfigurable surface topography for programming unidirectional liquid transport. *Adv. Funct. Mater.* **2019**, *29*, 1807858.

[20] Pang, K.; Ding, B. B.; Liu, X. T.; Wu, H.; Duan, Y. X.; Zhang, J. M. High-yield preparation of a zwitterionically charged chitin nanofiber and its application in a doubly pH-responsive Pickering emulsion. *Green Chem.* **2017**, *19*, 3665–3670.

[21] Cui, Y. D.; Li, D.; Gong, C.; Chang, C. Y. Bioinspired shape memory hydrogel artificial muscles driven by solvents. *ACS Nano* **2021**, *15*, 13712–13720.

[22] Liu, K. K.; Zhang, Y.; Cao, H. Q.; Liu, H. N.; Geng, Y. H.; Yuan, W. H.; Zhou, J.; Wu, Z. L.; Shan, G. R.; Bao, Y. Z. et al. Programmable reversible shape transformation of hydrogels based on transient structural anisotropy. *Adv. Mater.* **2020**, *32*, 2001693.

[23] Zhou, L. Y.; Fu, J. Z.; He, Y. A review of 3D printing technologies for soft polymer materials. *Adv. Funct. Mater.* **2020**, *30*, 2000187.

[24] Wang, Z. Y.; Gu, J. Y.; Zhang, D. F.; Zhang, Y.; Chen, J. H. Structurally dynamic gelatin-based hydrogels with self-healing, shape memory, and cytocompatible properties for 4D printing. *Biomacromolecules* **2023**, *24*, 109–117.

[25] Ding, Z.; Yuan, C.; Peng, X. R.; Wang, T. J.; Qi, H. J.; Dunn, M. L. Direct 4D printing via active composite materials. *Sci. Adv.* **2017**, *3*, e1602890.

[26] Zhao, W.; Yue, C. B.; Liu, L. W.; Liu, Y. J.; Leng, J. S. Research

progress of shape memory polymer and 4D printing in biomedical application. *Adv. Healthcare Mater.* **2023**, *12*, 2201975.
[27] Lu, H. H.; Wu, B. Y.; Yang, X. X.; Zhang, J. W.; Jian, Y. K.; Yan, H. Z.; Zhang, D. C.; Xue, Q. J.; Chen, T. Actuating supramolecular shape memorized hydrogel toward programmable shape deformation. *Small* **2020**, *16*, 2005461.
[28] Liu, Y. F.; Lv, Z. S.; Zhou, J. Z.; Cui, Z. Q.; Li, W. L.; Yu, J.; Chen, L. X.; Wang, X.; Wang, M.; Liu, K. Y. et al. Muscle-inspired formable wood-based phase change materials. *Adv. Mater.* **2024**, *36*, 2406915.
[29] Yang, C.; Zheng, W. Z.; Ni, C. J.; Li, Y.; Chen, D.; Xie, T.; Zhao, Q. Reconfigurable and orthogonal stiffness-structure patterning of dynamically crosslinked amphigels. *SmartMat* **2024**, *5*, e1255.
[30] Zhu, L. T.; Zong, L.; Wu, X. C.; Li, M. J.; Wang, H. S.; You, J.; Li, C. X. Shapeable fibrous aerogels of metal-organic-frameworks templated with nanocellulose for rapid and large-capacity adsorption. *ACS Nano* **2018**, *12*, 4462–4468.
[31] Huang, S. S.; Liu, D. Y.; Zhang, L. Y.; Zhang, Z. J.; Wang, S. X.; Zhang, W. J.; Duan, Y. X.; Zong, L.; Li, B. X.; Zhang, J. M. Harnessing squid bone for ultra-permeable water purification membranes. *Adv. Mater.* **2025**, *37*, e08514.
[32] Li, Z. H.; Li, Z. W.; Zhou, S. H.; Zhang, J. M.; Zong, L. Biomimetic multiscale oriented PVA/NRL hydrogel enabled multistimulus responsive and smart shape memory actuator. *Small* **2024**, *20*, 2311240.
[33] Zheng, Y. R.; Zhang, H.; Wang, Z. W.; Lu, A.; Yu, A. X.; Duan, B. Chitin nanofibrils assisted 3D printing all-chitin hydrogels for wound dressing. *Carbohydr. Polym.* **2024**, *334*, 122028.
[34] Kou, X. R.; Yang, Y. X.; Lu, Q. Y.; Ke, Q. F.; Zhang, Y. C. Controlled construction of ellipsoidal microcapsules via tannic acid/cellulose nanocrystal interfacial engineering. *Carbohydr. Polym.* **2025**, *369*, 124273.
[35] Panos, M.; Sen, T. Z.; Ahunbay, M. G. Molecular simulation of fibronectin adsorption onto polyurethane surfaces. *Langmuir* **2012**, *28*, 12619–12628.
[36] Pu, X. Q.; Wu, Y. Q.; Liu, J. Q.; Wu, B. H. 3D bioprinting of microbial-based living materials for advanced energy and environmental applications. *Chem Bio Eng.* **2024**, *1*, 568–592.
[37] Sun, H. N.; Hwang, U.; Kim, S.; Sung, J.; Kim, T.; Suhr, J.; Park, I. K.; Nam, J. D. Reversible thixotropic rheological properties of graphene-incorporated epoxy inks for self-standing 3D printing. *ACS Macro Lett.* **2025**, *14*, 135–141.
[38] Qiu, L.; Wang, Z. Y.; Liu, Z. H.; Li, H. M.; Feng, Y. H. Nanopore confinement-driven synchronous enhancement of thermal and mechanical properties of phase change materials. *Angew. Chem., Int. Ed.* **2025**, *64*, e202500957.
[39] Wang, Y.; Yuan, X. F.; Wang, J. J.; Wang, J. R.; Zhang, T.; Zheng, Y.; Xu, Y. T. Influence of confinement on the thermophysical property of paraffin wax/Kevlar nanofibrous phase change film. *J. Energy Storage* **2024**, *104*, 114553.
[40] Yang, Y. X.; Zhao, X. D.; Wang, S.; Zhang, Y. F.; Yang, A. M.; Cheng, Y. L.; Chen, X. S. Ultra-durable cell-free bioactive hydrogel with fast shape memory and on-demand drug release for cartilage regeneration. *Nat. Commun.* **2023**, *14*, 7771.
[41] Yarali, E.; Mirzaali, M. J.; Ghalayaniesfahani, A.; Accardo, A.; Diaz-Payno, P. J.; Zadpoor, A. A. 4D printing for biomedical applications. *Adv. Mater.* **2024**, *36*, 2402301.
[42] Zhu, Y.; Deng, K. C.; Zhou, J. W.; Lai, C.; Ma, Z. W.; Zhang, H.; Pan, J. Z.; Shen, L. Y.; Bucknor, M. D.; Ozhinsky, E. et al. Shape-recovery of implanted shape-memory devices remotely triggered via image-guided ultrasound heating. *Nat. Commun.* **2024**, *15*, 1123.
[43] Chen, X. M.; Feng, Y. H.; Zhang, P.; Ni, Z. P.; Xue, Y.; Liu, J. Hydrogel fibers-based biointerfacing. *Adv. Mater.* **2025**, *37*, 2413476.
[44] Zhu, P. A.; Wang, L. Q. Thermo-induced reversible nanoemulsification. *Matter* **2025**, *8*, 102103.
[45] Durgut, E.; Claeyssens, F. Pickering polymerized high internal phase emulsions: Fundamentals to advanced applications. *Adv. Colloid Interface Sci.* **2025**, *336*, 103375.
[46] Wang, Y. Q.; Zhang, Y.; Ren, P.; Yu, S. M.; Cui, P.; Nielsen, C. B.; Abrahams, I.; Briscoe, J.; Lu, Y. Versatile and recyclable double-network PVA/cellulose hydrogels for strain sensors and triboelectric nanogenerators under harsh conditions. *Nano Energy* **2024**, *125*, 109599.